photonics

MDPI

Article

Super-Resolution Structured Illumination Microscopy for the Visualization of Interactions between Mitochondria and Lipid Droplets

Ting He [1,2,3], Xuejuan Hu [1,2,3,*], Kai Hu [1,3], Jingxin Liu [4], Jiaming Zhang [1,3], Yadan Tan [1,3,5], Xiaokun Yang [1,3], Hengliang Wang [1,3], Yifei Liang [1,3,5], Shiqian Liu [3] and Jianze Ye [1]

1 Sino-German College of Intelligent Manufacturing, Shenzhen Technology University, Shenzhen 518000, China
2 College of Physics and Photoelectric Engineering, Shenzhen University, Shenzhen 518000, China
3 Laboratory of Advanced Optical Precision Manufacturing Technology of Guangdong Provincial Higher Education Institute, Shenzhen Technology University, Shenzhen 518000, China
4 College of Pharmacy, Shenzhen Technology University, Shenzhen 518000, China
5 College of Physics Science and Technology, Guangxi Normal University, Guilin 541000, China
* Correspondence: huxuejuan@sztu.edu.cn; Tel.: 0086+137-2863-4336

Abstract: Visualizing the dynamics of fine structures in cells requires noninvasive, long-duration imaging of the intracellular environment at high spatiotemporal resolution and low background noise. With modularized hardware and polarized laser modulation, we developed a nanoscale super-resolution structured illumination microscope (SR-SIM) imaging technique. Combined with a reliable image reconstruction algorithm and timing synchronization of all devices, the super-resolution (SR) images in hepatocytes reached 134.95 nm spatial resolution and 50 fps temporal resolution. This imaging system was able to maintain the optimal operation state over hundreds of time points due to less exposure and low phototoxicity. In hepatocytes, interactions between mitochondria and lipid droplets (LDs) underpin many crucial physiological processes, ranging from cellular metabolism to signaling. In this study, we pioneered the use of the SIM system for imaging the interaction characteristics between mitochondria and LDs. More than 200 hepatocytes were counted and recorded effectively. We found that LDs in an unstable state were divided under mitochondrial contact and fused without it. Among 200 LDs, more than 69% were surrounded by mitochondria that tended to wrap LDs. The SR-SIM imaging technique was demonstrated to break the limitations of conventional imaging methods in spatial-temporal resolution and imaging duration in the field of the dynamic study between mitochondria and LDs.

Keywords: super-resolution; SIM; hepatocyte; mitochondria; lipid droplets

check for updates

Citation: He, T.; Hu, X.; Hu, K.; Liu, J.; Zhang, J.; Tan, Y.; Yang, X.; Wang, H.; Liang, Y.; Liu, S.; et al. Super-Resolution Structured Illumination Microscopy for the Visualization of Interactions between Mitochondria and Lipid Droplets. *Photonics* **2023**, *10*, 313. https://doi.org/10.3390/photonics10030313

Received: 16 January 2023
Revised: 20 February 2023
Accepted: 10 March 2023
Published: 14 March 2023

Copyright: © 2023 by the authors. Licensee MDPI, Basel, Switzerland. This article is an open access article distributed under the terms and conditions of the Creative Commons Attribution (CC BY) license (https://creativecommons.org/licenses/by/4.0/).

1. Introduction

Conventional wide-field fluorescence imaging methods are limited by diffraction to ~200 nm lateral resolution (half of their wavelength), making it difficult to observe the fine structure within the organelle [1]. Confocal microscopy is most widely used in the visualization of microbial imaging. It eliminates out-of-focus background, but at the price of substantial photobleaching and reduced speed [2]. Relying on image processing or an improved setup, newer systems employing confocal microscopy approaches, such as Re-scan Confocal Microscopy [3] and Airy-scan (Zeiss), can provide 1.7× and 1.4× lateral resolution enhancement, respectively. However, issues common to these techniques are photobleaching and reduced speed [4]. To visualize potential organelle contacts with greater clarity over the long term, we must turn to SR fluorescence microscopy. The most popular and widely used SR fluorescence microscopy techniques are: Stimulated Emission Depletion (STED) microscopy based on point spread function compression [5,6], Structured Illumination Microscopy (SIM) based on spatial spectrum extension [7,8], and

Single-Molecule Localization Microscopy (SMLM) [9,10]. They show different imaging characteristics in the observation of the fine structure of cells [11]. Of the various forms of super-resolution, SIM is the best suited to combining high resolution with long-duration high-speed multi-color imaging, due to its low excitation intensity, use of conventional fluorescent labels, and the need for only nine two-dimensional raw images to reconstruct a super-resolution one [12–14].

Organelles interact with one another and synergistically execute various physiological functions [15,16]. Such interactions are increasingly recognized to be pivotal for diverse cellular functions [17]. When these interactions do not function properly, numerous pathologies, including infection and cancer, occur. Mitochondria bound to LDs have unique bioenergetics, compositional, and kinetic characteristics [18]. The study of interactions between LDs (lipid storage organelles) and mitochondria (lipid oxidation organelles) may be helpful to explore the pathogenesis and possible treatment of obesity-related metabolic disease. The fact that mitochondria adhere to LDs was confirmed by optical and biological methods [19–21]. Transmission electron microscopy (TEM) allowed the physical contact between two organelles to be observed in hepatocytes and other adipocytes [22,23]. The contact modes are related to the functions of two organelles, and the dynamics can be regulated [18,24,25]. The contact modes between mitochondria and LDs are summarized as "kiss and run" and "anchor" [26]. Whether or not they contact or how is related to a number of factors, such as the size of LDs [27]. Therefore, the interaction between mitochondria and LDs is regulated by many factors, which makes the dynamics between them complex and variable.

These discoveries were only possible with the advent of imaging technologies that allowed the dynamic organization of organelles to be studied. What is missing in dynamic research between mitochondria and LDs is an imaging technique with high spatiotemporal resolution yet low photobleaching and long-term imaging capability. Therefore, we developed SR-SIM. With a simple and rigorous architecture and an efficient timing synchronization controller, we were able to image dynamics between mitochondria and LDs at 134.95 nm resolution and 50 fps for hundreds of frames. Furthermore, multicolor SR images enabled us to make a quick statistical analysis of target organelles with a recognition detection algorithm. Thereby, we gained fresh insights into the spatial coordination between mitochondria and LDs, such as the association of LDs' fission and fusion with mitochondrion-LD (Mito-LD) contacts.

2. Materials and Methods

2.1. Optical Setup

In the case of incoherent imaging modalities (that image the incoherent light from the sample), such as fluorescence, the image intensity (E) detected by the detector is given as the convolution of the light intensity (I) from the sample and the point spread function (PSF) (h) of the imaging system:

$$\mathrm{E}(r) = (\mathrm{I} \bigotimes \mathrm{h})(r) \tag{1}$$

where (r) denotes the position vector on the detector and $\otimes$ represents the convolution operation. In general, the light intensity from fluorescent samples (I) is dependent on the sample structure (S) and the incident light intensity ($\mathrm{I_{in}}$):

$$\mathrm{I} = \mathrm{SI_{in}} \tag{2}$$

The fluorescence imaging system can be regarded as a low-pass filter. Only the low-frequency component within the cut-off frequency ($\mathrm{k_c}$) can pass through the imaging system smoothly and be detected. Figure 1b shows the typical optical transfer function (OTF). When the frequency is ($\mathrm{k_c}$), the OTF value of the PSF's frequency domain expression

is zero. Therefore, when we try to understand the image in the frequency domain, the signal detected by the camera can be expressed as:

$$\widetilde{E}(k) = (\widetilde{S} \bigotimes \widetilde{I}_{in})H(k) \quad (3)$$

where $(\widetilde{S})$, $(\widetilde{I}_{in})$, and (H) are the frequency spectra of the sample, the incident light, and the incoherent PSF, respectively.

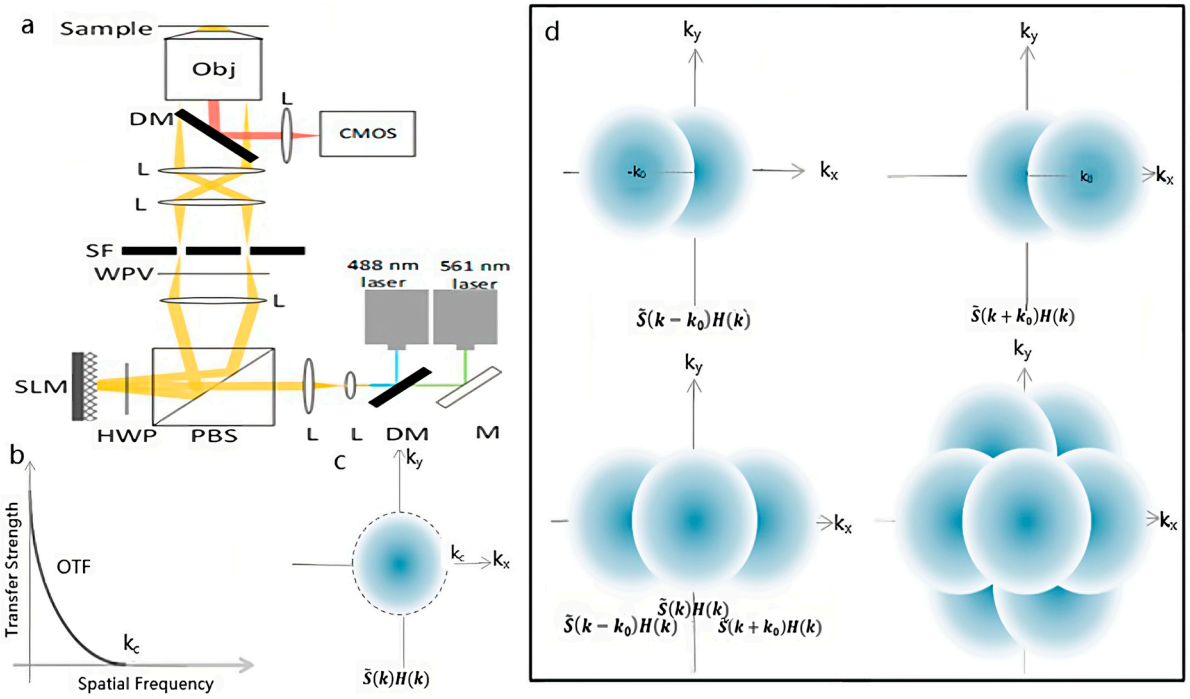


Figure 1. Optical setup: (**a**) Schematic diagram of the SR-SIM setup. M−Reflector; DM−Dichroic Mirror; l−Lens, PBS−Polarization Beam Splitter; HWP−Half-wave Plate; SLM−Spatial Light Modulator; WPV−Vortex Half-Wave Plate; SF−Space Filter. (**b**) Typical optical transfer function. (**c**) Frequency spectrum components of the object collected by the imaging system. (**d**) The shifted frequency spectrum components. Shifted frequency spectrum components of the object collected by the imaging system for a fringe pattern projected in one orientation (**upper**) and the reconstructed spectrum in that orientation (**lower left**); (**lower right**) represents the extended frequency spectrum of the object after assembling the similar parts in (**lower left**) for three different orientations of the projected fringe patterns.

When the illumination light with stripe patterns in the imaging system is used to excite the sample, the illumination field can be expressed as:

$$I_{in} = I_0[m\cos(2\pi k_0 + \varphi) + 1] \quad (m < 0.5) \quad (4)$$

(I_0) is the unit light intensity, (m), (k_0), and (φ) are the modulation depth, modulation frequency, and modulation phase, respectively. Therefore, the fluorescence field detected on the detector can be expressed as:

$$\widetilde{E}(k) = I_0\left[\widetilde{S}(k) + \frac{m}{2}\exp(i\varphi)\widetilde{S}(k - k_0) + \frac{m}{2}\exp(i\varphi)\widetilde{S}(k + k_0)\right]H(k) \quad (5)$$

Equation (5) shows the ability to extend the frequency domain of the optical imaging system by using structured fringe illumination, as shown in Figure 1d. When three structured fringe illumination samples in different directions are used, the resolution can be theoretically

improved by twice. In order to achieve a stable and efficient SR-SIM, we designed an optical path (Figure 1a) based on the interference fringe generation method. We detailed this optical system in Section 2.2.

The reconstructed frequency spectrum of the object has a cut-off at $k_0 + k_c$, which can be increased by increasing k_0, k_0, and kc are both limited by diffraction. For the case in which the sinusoidal pattern projected onto the object is through the interference of two plane waves, the maximum spatial frequency that can be generated is $k_{0\,max} = 2/\lambda_i$, where λ_i is the wavelength of the incident light. The maximum cut-off frequency is $k_{c\,max} = 2/\lambda_e$,where λ_e is the wavelength of the emitted fluorescence. As λ_e is slightly shifted by the Stokes shift, the maximum detectable frequency of the object is $k_{0\,max} + k_{c\,max} \approx 4/\lambda_e$. Hence, this technique can exceed the fundamental lateral resolution limit of the wide-field fluorescence microscope by a factor of 2.

2.2. SR-SIM System

The SR-SIM system consisted of four modules: a laser coupling module (black polygon in Figure 2), a structured pattern modulation module (blue polygon in Figure 2), a polarization rotation module (orange rectangle in Figure 2), and an image acquisition module (green rectangle in Figure 2). With a movable custom optical breadboard (MBB-SP-1, LBTEK, Changsha, China), modular grouping allowed the system to move and assemble at any time. The system was based on a commercially available inverted fluorescence microscope (IX83, Olympus) [28] equipped with a high numerical aperture (NA) objective (UPLXAPO100XO, Olympus, Tokyo, Japan). The first was a laser coupling module. Two lasers were used in this system (488 nm, Cobolt 06-MLD 100 mw, and 561 nm, Cobolt 06-DPL 100 mw, Stockholm, Sweden) as light sources. Reflectors (BB1-E02, Thorlabs, Newton, NJ, United States of America), a beam splitter (EBS1, Thorlabs), and a climbing frame (RS99M, Thorlabs) were then set up to combine laser beams. Laser beams were expanded to 4.5 cm in diameter through 2 4F systems. Two 4F systems consist of four lenses (f = 7.5 mm, AC050-008-A-ML; f = 150 mm, AC254-150-A-ML; f = 30 mm, AC254-030-A-ML; f = 100 mm, AC254-100-A-ML, Thorlabs) with an adjustable diaphragm (SM1D12C, Thorlabs) installed in the middle. The output lasers were then diffracted by a pure phase grating consisting of a polarizing beam splitter cube (CCM1-PBS251/M, Thorlabs), a ferroelectric liquid crystal spatial light modulator (QXGA-3DM, Fourth Dimension Display, Fife, United Kingdom) [14], and an achromatic half-wave plate (AHWP10M-600, Thorlabs). The diffraction beams were focused by another achromatic lens (f = 500 mm, AC254-500-A-ML) onto the intermediate pupil plane, where a carefully designed stop mask was placed to block the zero-order beam and other stray light and to permit the passage of ± 1 order beam pairs only. The pure phase grating and stop mask constituted the structured pattern modulation module. We placed a zero-order vortex half-wave plate (WPV10-532, Thorlabs) after the stop mask as a polarization rotator to maximize the modulation contrast of the illumination pattern while eliminating the switching time between different excitation polarizations [29]. The specific modulation process is shown in Figure 3b. The modulated incident beams then passed through another 4F system consisting of 2 identical lenses (f = 300 mm, AC254-300-A-ML) and several mirrors, which was polarization rotation module. Lasers were coupled into the fluorescent lamp group of the inverted microscope. Thus, the fluorescent illuminator and mercury lamp box had to be removed in advance. The dichroic mirror (ZT405/488/561/640rpc-phase R-UF, Chroma, Bellows Falls, VT, United States of America) in the microscope body used to reflect the illumination beams was designed with low polarization dependence so that the orthogonal relationship between polarization state and pattern wave vector was maintained. After focusing on the back focal plane of the objective lens, the light passed through the lens and interfered with the sample plane. The emitted fluorescence collected by the same objective passed through a dichroic mirror, an emission filter, and a tube lens in the microscope body. The emitted fluorescence was then captured by a scientific complementary metal-oxide semiconductor camera (sCMOS)

(KURO2048 × 2048, 11 µm, Princeton Instruments, Trenton, NJ, United States of America). The microscope and sCMOS constituted the image acquisition module.

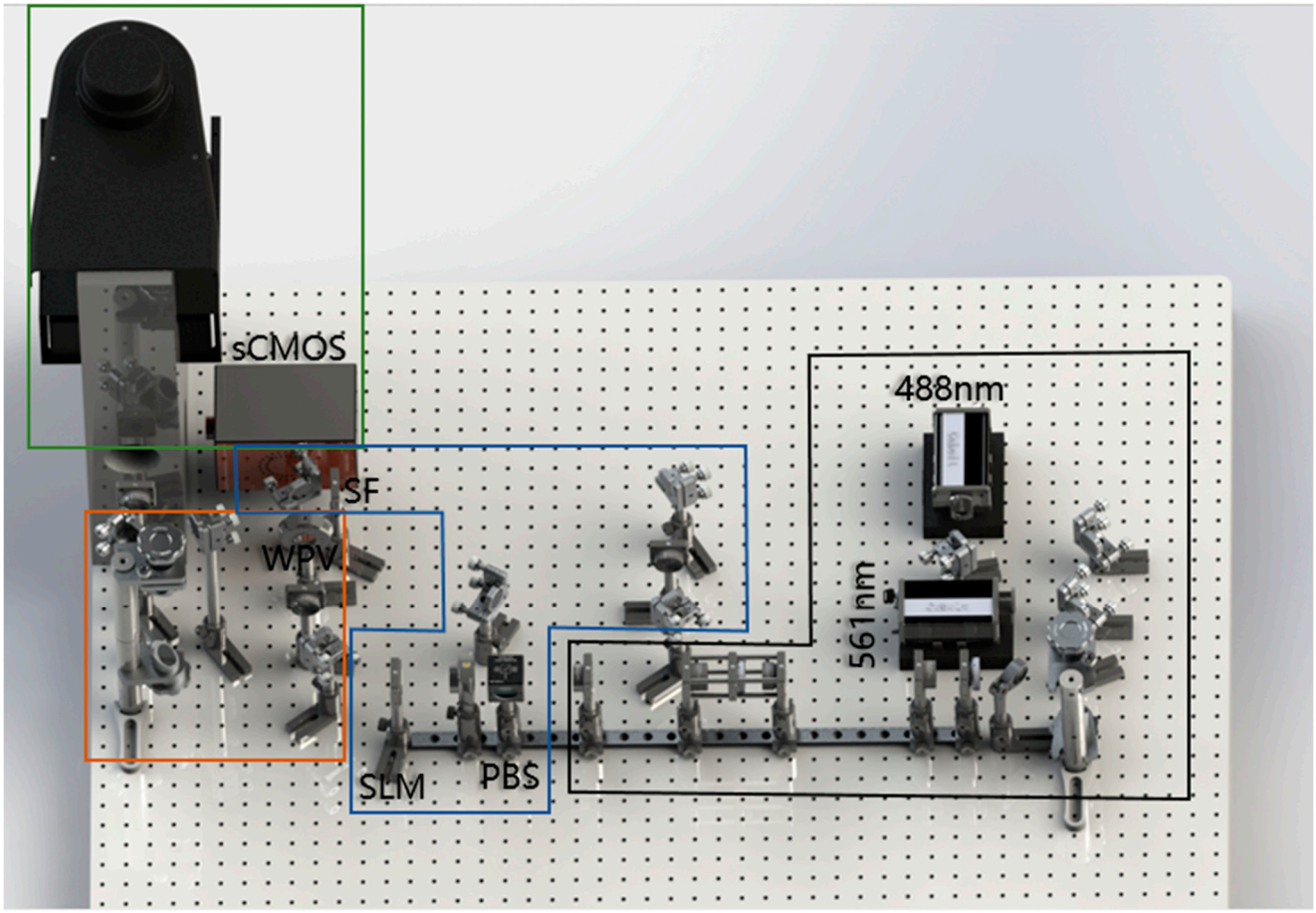


Figure 2. System construction.

The key to the SR-SIM system is the generation of controllable structural stripes. In our setup, the interference patterns for SIM were generated by displaying a periodic pattern on a ferroelectric liquid crystal SLM [30]. The gratings were designed and characterized based on the available code from Markwirth, A. et al. [31]. The period, phase, and orientation of the illumination patterns were modified by writing different pixel patterns. The spacing of the patterns was adjusted for each color to generate the diffraction spots in the same position in the Fourier plane, so that the light can pass the stationary spatial filter mask without switching spatial filters. Therefore, all wavelengths yielded the same relative resolution improvement [31]. According to a previous study [32], nine raw frames illuminated with a periodic pattern of parallel lines and shifted through three phases for each of the three orientation angles were required to reconstruct one SR image. For SR-SIM, the pupil radius of the annulus on the back focal plane of the objective lens was 1.8 mm, and the position and distribution of the small holes on the spatial filter mask were designed according to the imaging relationship. The relay lens system in the excitation path gave access to the SLMs' Fourier plane and allowed them to filter out these unwanted orders with a simple mask. The modulation contrast of grating patterns in SLM was 1, and pattern periods were 15 pixels (0°) for the 488 nm laser and 16 pixels (0°) for the 561 nm laser. With 3 orientations and 3 phase shifts, the ±1 order diffraction lights were projected at the specific position of the mask. In order to maximize the modulation contrast of the interference fringes, it was necessary to change the polarization of the two input beams to S-polarization. Thus, a zero-order vortex half-wave plate was installed as a polarization rotator, whose

fast axis distribution is shown in Figure 3b. For example, to obtain the red interference fringes (Figure 3d) with high contrast, the polarization directions of the two interference beams had to be parallel to the orientation of the red fringes. When the S-polarized light (Figure 3(c_i)) projected onto the WPV at the red spot position, the fast axis distribution at the red spot (Figure 3(c_{ii})) modulated the polarization direction to the target polarization direction (Figure 3(c_{iii})). The interference fringes in other orientations were modulated similarly. After passing through the WPV, the linearly polarized light beams illuminating different positions on the plate rotated the orientation of polarization, which eliminated the switching time between different illumination polarizations.

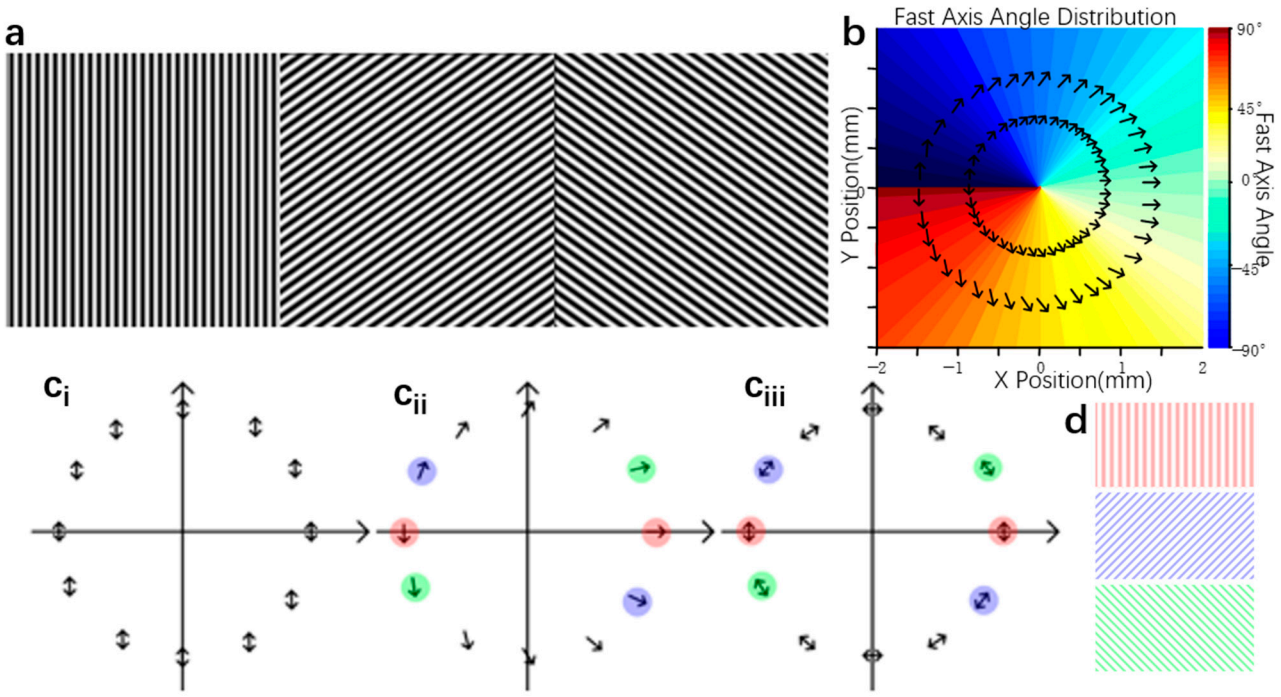


Figure 3. Principle of structural fringe modulation: (**a**) Three orientation fringe patterns loaded on the spatial light modulator (**left: 0°, medium: 60°, right: −60°**). (**b**) The schematic diagram of the fast axis distribution of the zero-order vortex half-wave plate. (**ci**) The arrows represent polarization direction of the incident light; (**cii**) the arrows represent fast axis direction of the WPV, where different colors (**red, blue, and green**) represent the position of the ±1 order diffracted light projected on the WPV after the incident light is diffracted by the three grating images in (**a**); (**ciii**) the arrows represent polarization distribution of the outgoing light modulated by the WPV. (**d**) The interference fringes in the sample plane.

2.3. Cell Culture and Treatments

AML12 cells were purchased from the American Type Culture Collection (Rockvile, MD, USA), and cultured in DMEM medium supplemented with 10% FBS and ITS-G (insulin 5 mg/mL, transferrin 5 mg/L, selenite 5 μg/L, Shanghai Peiyuan Biotechnology, Shanghai, China) in humidified air containing 5% CO_2 at 37 °C. Oleic and palmitic acids were then completely dissolved in 75% ethanol by heating at 55 °C. The prepared fatty acid solution was re-added into the cell culture medium to prepare a fatty acid working solution (P/O solution) with sodium oleate and palmitic acid concentrations of 500 μM and 250 μM, respectively. The solution was placed in a shaker incubator for 2 h and sterilized with a 0.2 μm filter membrane. For lipid droplet induction, the original cell culture medium was discarded and replaced with P/O solution for 12 h, followed by other operations, such as immunofluorescence.

2.4. Immunofluorescence

AML12 hepatocytes were seeded in a confocal culture dish and stained with Mitotracker Red CMXRos and Bodipy 493/503 for mitochondria and LDs, respectively. After being incubated for 15 min at 37 °C and then washed with PBS three times, the self-made SR-SIM imaging system was used to observe mitochondria and LDs with excitation wavelengths of 561 nm and 488 nm, respectively. For the stained hepatocytes, nine original monochromatic images of red (mitochondria) and green (LDs) were then alternately captured.

2.5. Reconstruction Algorithm

The raw images were first processed using ImageJ software (v 1.52a). A plugin of ImageJ named SIMcheck was used to examine the quality of the raw images obtained using the SIM microscope. After estimating the reconstruction parameters (pattern wave vectors [33], starting phase, and modulation depth [34]), the Wiener parameters that were calculated by SIMcheck were used for the Wiener deconvolution algorithm. The improved algorithm based on the Wiener SIM reconstruction algorithm was combined with an adjustable notch filter to reduce background (almost no background).

3. Results

3.1. Hardware Implementation

Modular hardware structures were independent while cooperating with each other. Such as the SLM in the structured pattern modulation module, it was used to display images with a temporal resolution from 0.2 milliseconds (ms) to 56 ms and a spatial resolution of 1280 × 1024 pixels on a 20.68 mm × 18.87 mm reflection mode silicon die (active area 17.43 mm × 13.95 mm) microdisplay, which regulated the diffraction beams quickly and precisely. To obtain the optimal trade-off between resolution and photon budget, we used a high NA objective and a sCOMS camera with 95% peak quantum efficiency in the image acquisition module to detect emission fluorescence. WPV was used to rotate polarization direction in real time, which provided high-contrast illumination stripes and lossless polarized light utilization, as well as lossless temporal resolution. Additionally, we designed a synchronization paradigm that efficiently coordinates the pattern generation of the SLM and the camera readout interval [35]. The SIM system was developed with high time resolution and long-term imaging capability. Lipid metabolism in hepatocytes was interesting and mysterious, closely related to the interactions between mitochondria and LDs. We demonstrated the superior imaging capability of SR-SIM by dynamic imaging of mitochondria and LDs and further obtained some morphological features of the interactions between mitochondria and LDs.

3.2. System Characterization

Since all factors that influenced the resolution corresponded to changes in the transmission of the frequencies and the noise level, the Fourier Ring Correlation (FRC) analysis was sensitive to all these factors. Given two images of the same field of view but with independent noise realizations (independent images), the FRC analysis allowed us to retrieve the effective cut-off frequency of the images with no prior knowledge or calibration. In a nutshell, the FRC measured the degree of correlation of the two images at different spatial frequencies (Figure 4). The resulting curve was close to unity at low spatial frequencies; for spatial frequencies higher than the effective cut-off frequency, non-correlated (independent) noise realization dominated and the curve approached zero. The effective cut-off frequency was the frequency at which the correlation curve dropped below a given threshold (Figure 4b). The FRC analysis was a plugin of ImageJ [36]. Improved algorithm based on the Wiener SIM reconstruction algorithm using an adjustable notch filter to remove the defocused signal and its artifacts. Combined with the high numerical aperture afforded by a commercially available 1.45-NA objective, a spatial resolution of 134.95 nm (emission wavelength at 600 nm) compared to a resolution of 287.35 nm in wide field imaging was

achieved (Figure 4). Better spatial resolution would be obtained with blue-shift emission [1]. Therefore, the two-color images were obtained with a spatial resolution of sub-134.95 nm by this SIM system.

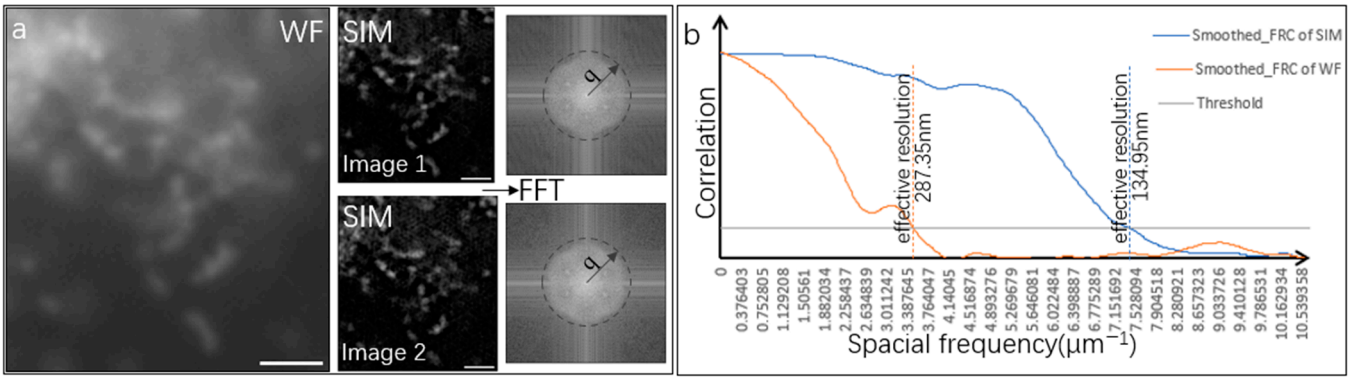


Figure 4. System calibration: (**a**) Using a wide field image (**left**) and SIM images (**middle**) for mitochondria, the correlation between the Fourier transforms of the two independent images (**right**) over the perimeter of the circle of radius q is calculated, resulting in a FRC curve indicating the decay of the correlation with spatial frequency. (**b**) The image resolution is the inverse of the spatial frequency for which the FRC curve drops below the threshold 1/7~0.143, so a threshold value of q = 7.4 μm^{-1} is equivalent to 134.95 nm resolution (excitation wavelength at 561 nm, emission wavelength at 600 nm). Scale bar: 1.5 μm.

Live-cell SR imaging at ms temporal resolution was challenging due to the amount of emission photons that needed to be collected during such short exposures. To avoid fluorescence quenching due to phototoxicity and questionable fidelity caused by a low signal-to-noise ratio, the raw images are captured during 20 ms exposures from a 56.32 μm × 56.32 μm field of view (FOV). The grating patterns in SLM are displayed recurrently with a digital signal cycle of 20 ms. First of all, DAQ sent a digital signal to activate SLM so that it displayed grating patterns in a period of 20 ms. The rising edge of the digital signal from SLM triggered the camera to expose for 20 ms with an initial delay of 0.05 ms. For multi-color images, after 27 time points, a digital signal was sent to switch filters and lasers. Continuous imaging during 20-ms exposures balanced low background and low phototoxicity. Guaranteed sufficient sampling rate to capture the details of organelle activation without motion artifacts caused by long exposures (Figure 5). The large FOV ensured high efficiency (2 or 3 complete cells per image). The rolling reconstruction of raw images was designed based on the ideas from Huang et al. [37] and achieved a time resolution of 50 fps for monochromatic imaging, while dual-color imaging required an extra 6 s to replace the filters.

In our setup, the excitation laser power in sample plane was approximately 26.6 W/cm^2. To prove the long-term imaging ability of the SR-SIM system, we captured 15 groups of raw images of mitochondria at a speed of 1 group per minute. Reconstructed SR images were compared with the confocal images obtained under the same conditions (Figure 6). Figure 6c,d show the normalized intensity of mitochondrial fluorescence. The SIM images not only had a low background but also barely quenched fluorescence over 15 min (Figure 6b). Although the uneven distribution of the fluorescent intensity was caused by the bias of the illumination angle, the fact that the signal was available to be continuously detected could not be ignored. However, confocal images produced significant fluorescence decay as exposure times increased from "Time Point 0" to "Time Point 14" (Figure 6c, T0–T14), as the illumination intensity of conventional point-scanning confocal microscopy was ~kW/cm^2 [38]. The illumination intensity of the SIM system was far lower than that of the confocal microscope, which led to indistinct fluorescence quenching and proved the long-term imaging ability of the SR-SIM system.

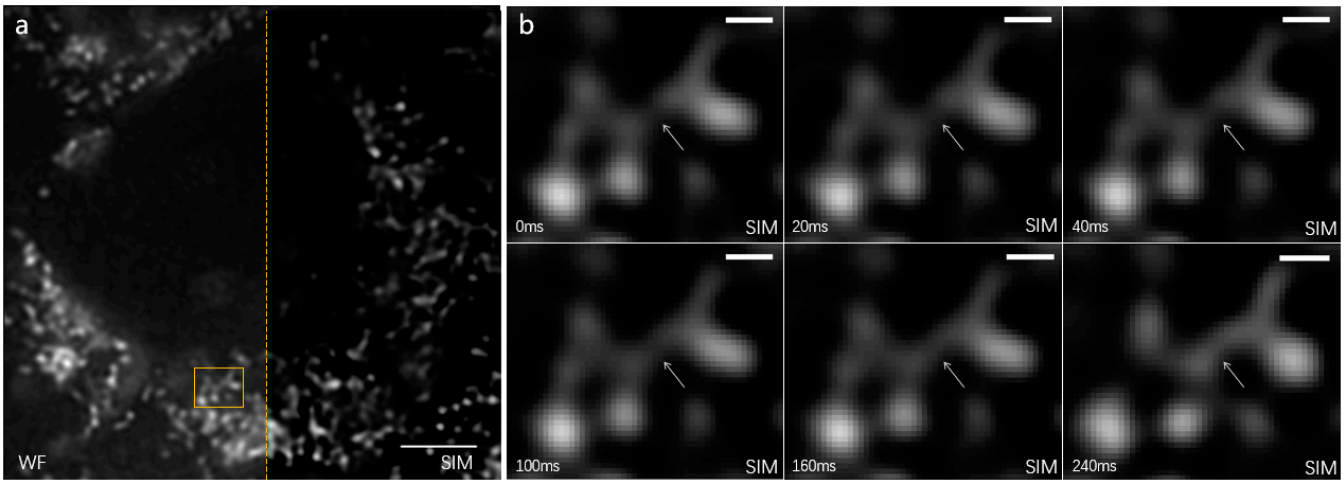


Figure 5. SR-SIM in resolving mitochondrial tiny movement under 20 ms exposures: (**a**) The left and right sides of the dotted line are the wide-field image and the SR image, respectively. (**b**) In the enlarged SR images of the yellow rectangle in (**a**), white arrows show the fusion of mitochondria within 240 ms. Scale bar: 4 μm in (**a**), 0.5 μm in (**b**).

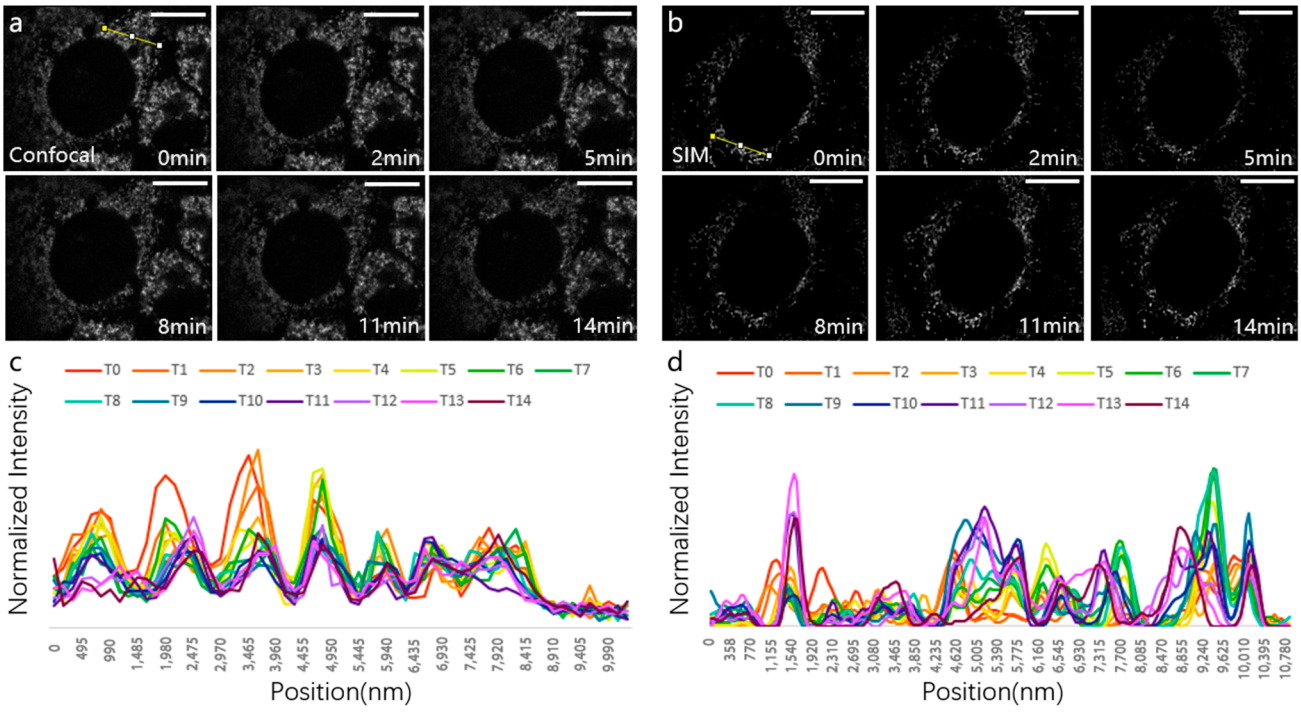


Figure 6. Comparison of SIM and confocal microscopy for long-time imaging. (**a**) Confocal images of mitochondria for 15 min. (**b**) SIM images of mitochondria for 15 min. (**c**) Normalized intensity distribution across the yellow line in (**a**). (**d**) Normalized intensity distribution across the yellow line in (**b**). Scale bar: 10 μm.

3.3. Fission and Fusion of Lipid Droplets Links to Mitochondrial Mediation

By using the SR-SIM to image hepatocytes, we clearly observed the fission and fusion processes of LDs in SR images (Figure 7a–d, lower). Due to the limitation of resolution, these processes of LDs were difficult to identify in wide-field images (Figure 7a–d upper). In addition, we noticed that the vast majority of LDs were stable without obvious dynamic changes. Very few LDs have been separated and fused under special circumstances. Interestingly, we found that the fission and fusion of LDs were linked to mito-LD contacts. In the

fission events of LDs, LDs were anchored by mitochondria (Figure 7a,b). In fusion events of LDs, mitochondria were absent (Figure 7c,d). Moreover, we observed that small ones separated from large ones in fission events, and fusion events occurred between two large LDs. Furthermore, we noticed that the fission processes of LDs were accompanied by several leaving and approaching events (Figure 7a,b), and the fusion processes were the continuous approaching of two LDs (Figure 7c,d). Last but not least, there was a significant difference between the fission and fusion duration of LDs; the duration of the fission events of LDs that were associated with mito-LDs contacts was longer than that of the fusion events without mitochondrial involvement (Figure 7e). These observations suggested that the fission and fusion of LDs were modulated by a number of factors, including mito-LD contacts.

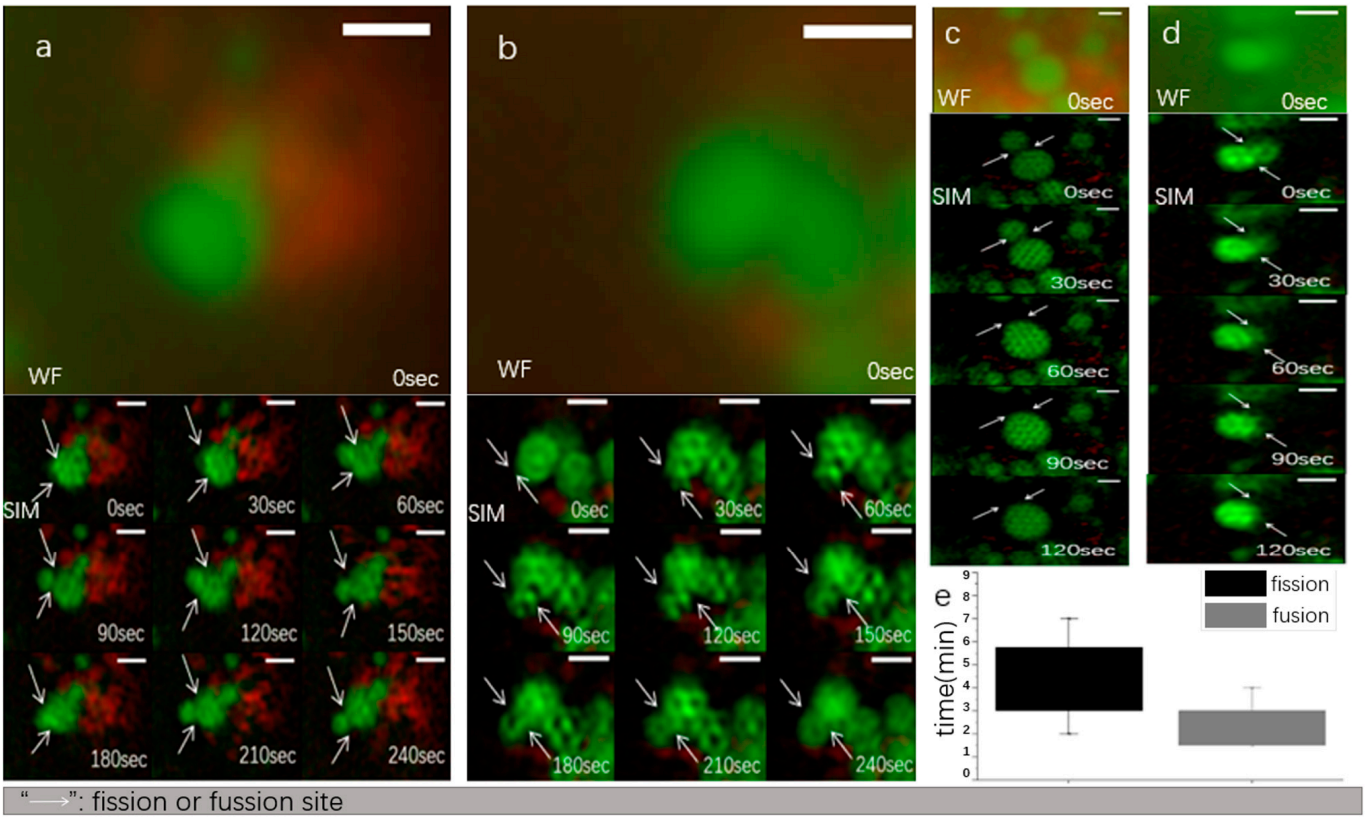


Figure 7. Fission and fusion of LDs: (**a**,**b**) Fission of LDs. (Top) of (**a**,**b**) are the original wide-field images; the rest are the super-resolution images. (**c**,**d**) Fusion of LDs. (Top) of (**c**,**d**) are the original wide-field images; the rest are the super-resolution images. (**e**) Comparison of the duration of LDs' fission and fusion. Scale bar: 1 μm.

We scrutinized 18 cases of LDs' fission and 15 cases of LDs' fusion from 120 cells. We surprisingly found that mito-LD contact was involved in 100% of fission events and absent in 100% of fusion events. During fission events, mitochondria were in close contact with the target LDs, and the contact state was maintained until the division occurred to give two independent LDs. Figure 7a,b show two typical fission modes of LDs. The position pointed at by the arrows germinate new LD on the surface of the large LD under the mediation of mitochondria (Figure 7a lower). The swallow back events are displayed during the fission process (120 and 180 s in Figure 7a). Within 4 min of tracking the fission of the LDs, the new LD pointed by the arrows is shown germinating and growing (Figure 7b). After 90 s, the two LDs are relatively stationary, neither swallowing nor separating into two independent LDs (90–240 s in Figure 7b). We therefore inferred that the process of LD fission was related to the mito-LD contact site and contact area. Figure 7c,d show two typical fusion modes of LDs. The fusion sites pointed by arrows show a fast and straightforward fusion process (Figure 7c) and a uniform merger (Figure 7d) without mito-LD contact. LDs' fusion is

regulated by many factors, such as surface tension, LD size, and protein mediation [27,39]. This may be the reason for the differences in fusion processes. We quantified the duration of all the fission events by measuring the time from the first sprouting until they were divided into two independent LDs. We quantified the duration of all the fusion events by measuring the time from the first contact of two LDs until complete relaxation of the post-fusion constriction. We found that LDs fission events with mitochondrial involvement took on average longer compared to fusion events (Figure 7e). On rare occasions, we observed that the fission of LDs lasted for 3 to 6 min and the fusion of LDs lasted for 1.5 to 3 min.

3.4. Mitochondria Move toward Lipid Droplets and Enwrap Lipid Droplets

Mitochondria were active according to a lot of images. Not only do mitochondria separate and fuse frequently, but they also move around in the cytoplasm and interact with other organelles. In super-resolution images, we observed the mitochondrial dynamic motion (Figure 8a, left) and identified the contact sites of mito-LD contacts (white arrows in Figure 8a). In addition, we found that mitochondria moved toward adjacent LDs and made contact with LDs. Mitochondria tended to approach larger LDs than smaller ones. The contact processes between mitochondria and LDs were summarized as two modes: "kiss and run" and "anchor" [26]. Interestingly, we found that as "kiss and run" and "anchor" both occurred between LDs and mitochondria, the mitochondrial density around LDs increased (Figure 8b,c). These observations suggested that the interaction and proximity trends of these two organelles were simultaneous. Furthermore, we found that mitochondria encapsulated LDs stably in some hepatocytes (Figure 8d). The hypothesis of permanent binding of two organelles held that in some oxidized tissues, mitochondria were anchored to LDs and formed permanent complexes [40]. We thus speculated that mitochondria tended to move closer to LDs and encapsulated LDs, and this dynamic between mitochondria and LDs might be related to the interaction function of two organelles.

We developed recognition detection algorithms and designed statistical methods to quantify the interactions between mitochondria and LDs. Circles were placed around the LDs, and the inner walls of these circles were 10 pixels away from the outer surface of the LDs. We then defined the circles as the neighborhood of LDs (white circles in Figure 8b). We counted the number of pixels occupied by mitochondria in the neighborhood of LDs and represented the density of mitochondria around LDs with the pixels' number. The degree of closeness between LDs and mitochondria was expressed by the mitochondrial density variation. After mitochondria and LDs in the region of interest (ROI) were identified and detected, we selected the target LDs in the ROI and calculated the mitochondrial content changes in their neighborhood. We scrutinized 200 LDs from 120 cells and counted the mitochondrial density in their neighborhood within 5 min at a time interval of 30 s. We plotted the mitochondrial density around the LDs into a line chart as shown in Figure 8e and performed linear fitting. It was worth noting that the slope of the fitted lines represented the trend of mutual movement between mitochondria and LDs. We took the slope between -5 and 5 as the demarcation point of the mutual movement between mitochondria and LDs (Figure 8f). The fitted lines with slope between -5 and 5 were considered to represent stable contacts between two organelles. The fitted lines with a slope of less than -5 meant that mitochondria moved in the opposite direction from LDs. The fitted lines with a slope greater than 5 indicated that the mitochondrial density increased and that mitochondria were approaching LDs.

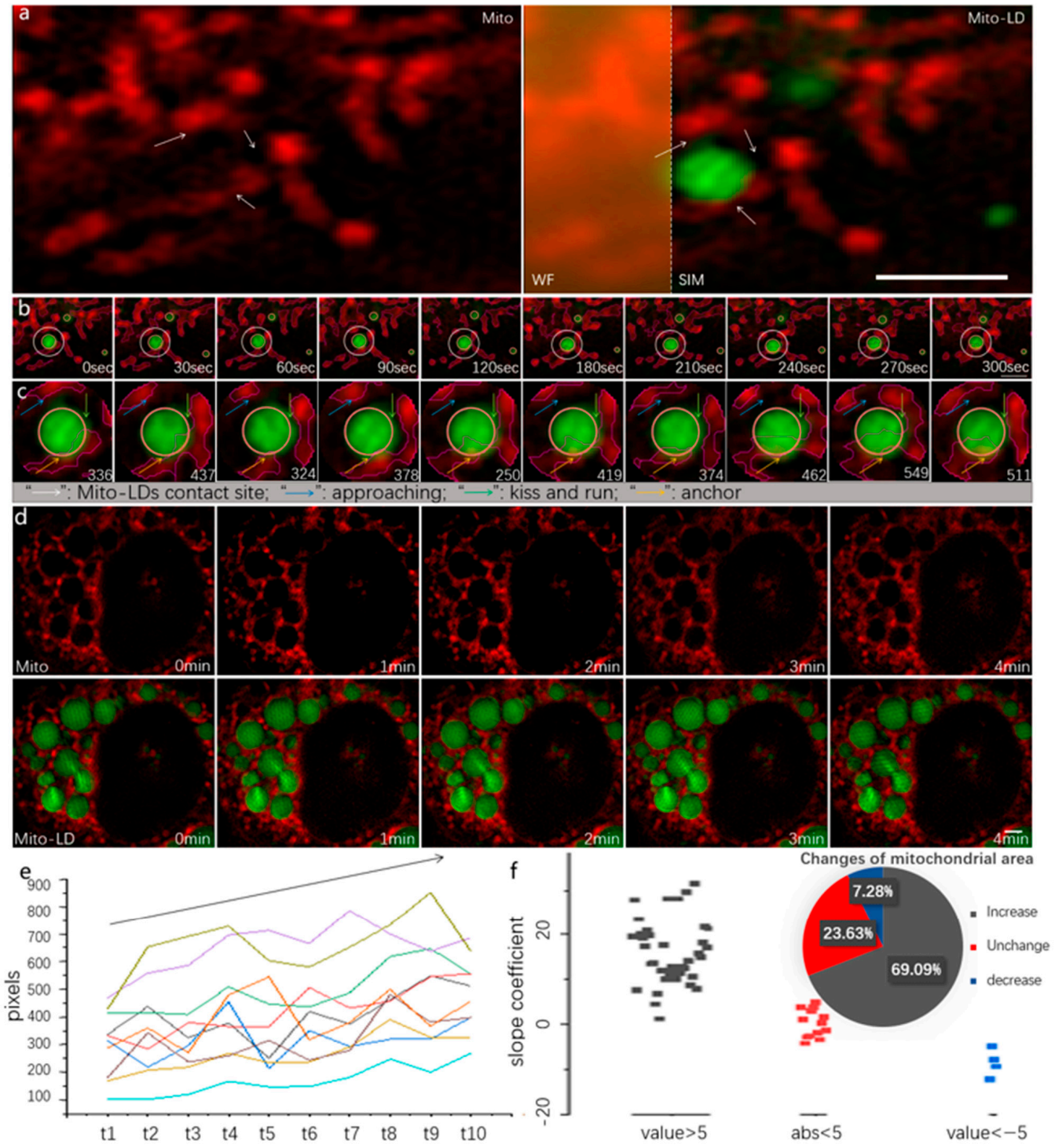


Figure 8. Mitochondrial movement to adjacent LDs: (**a**) Contact sites between mitochondria (**red**) and LDs (**green**) in AML12 cells, mitochondria (**left**) with pre-contact points and mito-LD contact (**right**), (**b**) Mitochondria and LDs detected at different times are pointed out in (**a**); (**c**) an enlarged picture of the circle is shown in (**b**). The numbers in the lower right are the pixels occupied by mitochondria (**red**), and arrows in different color represent different mito-LD contact modes. (**d**) Schematic of mitochondria-encapsulated LDs. Mitochondria with holes (**upper**) and mitochondria with holes filled by LDs (**lower**). (**e**) Trends in the number of mitochondria in the LDs' neighborhood over time, and the different line represent different LD. (**f**) The proportion of changes in the number of mitochondria in LDs' neighborhoods. Scale bar: 2 μm.

Nanoscale resolution and low background images allowed us to identify all mitochondria and LDs in the ROI. High-speed and long-duration imaging techniques allowed us to track the dynamic process between two organelles. We thus recorded a typical process of mitochondria approaching LDs (Figure 8b,c). We counted the number of pixels of mitochondria in the LD's neighborhood at 10 different time points and recorded the values in the lower right of the images (Figure 8c). Different contact modes between mitochondria and LDs can be seen in the image, such as "kiss and run" (green arrows in Figure 8c) and "anchor" (yellow arrows in Figure 8c). Combined with the numerical changes in the lower right, it can be inferred that the approaching trend (blue arrows in Figure 8c) between mitochondria and LDs coexisted with "kiss and run" and "anchor". Upper in Figure 8d shows the mitochondrial dynamics for 5 min, and there are many holes formed by mitochondria. These holes are perfectly filled by LDs (Figure 8d lower). A rising line chart of mitochondrial density in the neighborhood of 10 randomly selected LDs shows the proximity of mitochondria around LDs (Figure 8e). The slope of the fitted lines from randomly selected 50 LDs also indicates the fact that mitochondria move toward the LDs (Figure 8f). More than 69% of mitochondria have a tendency to move towards LDs and wrap LDs, and 23.63% of mitochondria are in stable contact with LDs, as shown in the pie graph in Figure 8f. We believed that the stable form of mitochondria wrapping LDs was the result of mitochondria approaching and interacting with LDs, and we inferred that Mito-LD permanent complexes might eventually form. Dynamic contact between mitochondria and LDs may transition to stable contact as energetic requirements fluctuate. There may be other important structural and functional differences between stable contact and flexible engagement.

4. Discussion

The SR-SIM described in this paper offered a combination of super-resolution, high-speed, multicolor imaging, low photobleaching, and low phototoxicity that made it well suited for studying intracellular dynamics. Compared with conventional imaging methods, it provided ~2× better spatial resolution and a faster imaging speed. Meanwhile, compared with other super-resolution methods, it better balanced the trade-off between high spatial and temporal resolution and the low photobleaching and phototoxicity of live cell imaging in a cell-sized field of view. This SR-SIM set up with a temporal resolution of 50 frames per second for monochromatic imaging and a lateral resolution of 134.95 nm, proved to be very suitable for studying interactions between mitochondria and LDs.

The diameter of mitochondria in mouse hepatocytes was mostly about 0.5~1 μm, and the diameter of LDs that were treated by P/O were mostly more than 0.5 μm. The shapes of mitochondria and LDs were larger than twice the spatial resolution, thus the movements of these two organelles would be captured without miscounting the interactions. However, the overlap between mitochondria and LDs in 2D images that did not make actual physical contact could cause misinterpretation. Since the spatial resolution of the z-direction was limited to ~600 nm [1], misinterpretation might occur in the longitudinal direction. However, the movements in the xy-direction were determined, and the clear fluorescence signal ensured that there were barely any movements in the z-direction. Thus, the conclusion about interactions between mitochondria and LDs was correct based on the analysis of the obtained data. The results showed that most of the LDs in P/O-treated hepatocytes were in a stable state for a long time after P/O incubation stopped. However, a small number of LDs still behaved actively in some specific cases, such as the fission of LDs in the case of mitochondrial mediation and the fusion of LDs without mitochondria. This might relate to the function of the interaction between the two organelles. Proper regulation of cellular lipid storage and oxidation is indispensable for maintaining cellular energy homeostasis and health. Mitochondria are the main determinant of functional lipid storage and oxidation. Since the LDs split into two independent, smaller ones with mito-LDs contacts, we speculated that tiny LDs could be completely decomposed under the action of mitochondria. Therefore, our results supported the conclusion that mitochondria

were responsible for LDs oxidation. This study also showed that the mitochondria had a tendency to approach the adjacent LDs and tend to gradually wrap the LDs. Additionally, the "approaching" coexisted with "kiss and run" and "anchor", which meant there might eventually be organelle complexes. This observation was consistent with the "anchoring assumption" that dynamic contact could transit to stable contact as energetic requirements fluctuate. Alternatively, if these were permanent states of association, there might be other important structural and functional differences between these two states. Thus, both morphological and biochemical methods should be used together to study the contact between LDs and mitochondria as well as other organelle contacts.

Further improvements in SR-SIM technology can be envisioned. Firstly, it may be possible to decipher events in the 3D intercellular structure of the whole cell, at the cost of requiring more raw images. 3D-SIM may also bring some problems, such as system complexity and difficulty in image processing. In addition, spectral unmixing methods can be developed to achieve multi-spectral super-resolution imaging of the mutual interactions of six or more organelles simultaneously. Moreover, new fluorescent probes can be used to characterize the changes of key proteins while different organelles interact, which might increase the requirements for fluorescent samples and require the development of integrated processing modules for multi-spectral images.

5. Conclusions

In summary, the SR-SIM method developed and implemented in this study meets some of the requirements for intracellular dynamic imaging, with ultra-high spatial (134.95 nm) and temporal resolution (50 fps) and minimal invasiveness. According to our results, mitochondria supported LD oxidation rather than expansion. Dynamic contact between mitochondria and LDs might shift to stable contact as energetic requirements fluctuate. These observations carried out using SR-SIM in this study revealed that the dynamics between mitochondria and LDs were complex, mysterious, and worth exploring. The SR-SIM imaging technique, combined with recognition detection algorithms and statistical methods, provided a more affordable and accessible visualization tool for the kinetics study in the field of dynamic study between mitochondria and LDs. Thus, it opens a new window and provides a near-perfect description tool for the study of highly dynamic interactions within cultured cells or cells at the periphery of multicellular organisms. It also inspires the further study of mitochondria and LDs with biological and morphological methods.

Author Contributions: Conceptualization, X.H. and J.L.; Methodology, T.H.; software, K.H.; validation, T.H. and J.Z.; formal analysis, K.H., H.W., J.Y.; investigation, T.H., K.H., and Y.L.; resources, X.H., J.L.; data curation, T.H. and K.H.; writing—original draft preparation, T.H. and X.Y.; writing—review and editing, X.H., S.L., and J.L.; visualization, T.H., K.H., and Y.T.; supervision, X.H.; project administration, X.H.; funding acquisition, X.H. All authors have read and agreed to the published version of the manuscript.

Funding: This research was funded by the Characteristic Innovation Project (Natural Science) of Ordinary Colleges and Universities in Guangdong Province (Grant No. 2021KTSCX111), the Shenzhen Pingshan District Science and Technology Innovation Special Supporting Project (Grant No. PSKG202006), the Self-made Instrument Project of Shenzhen Technology University (Grant No. JSZZ202102023), and the Stable Support Fund for Higher Education Institutions of Shenzhen (general project) (Grant No. 20220718183230002).

Data Availability Statement: New data were unavailable due to privacy.

Acknowledgments: We thank Lingling Chen for commenting on the optics and biological experiments.

Conflicts of Interest: The authors declare no conflict of interest. The funders had no role in the design of the study; in the collection, analyses, or interpretation of data; in the writing of the manuscript; or in the decision to publish the results.

References

1. Abbe, E. Beiträge zur Theorie des Mikroskops und der mikroskopischen Wahrnehmung. *Archiv f. mikrosk. Anat.* **1873**, *9*, 413–468. [CrossRef]
2. Sandison, D.R.; Piston, D.W.; Williams, R.M.; Webb, W.W. Quantitative comparison of background rejection, signal-to-noise ratio, and resolution in confocal and full-field laser scanning microscopes. *Appl. Opt.* **1995**, *34*, 3576–3588. [CrossRef] [PubMed]
3. De Luca, G.M.; Breedijk, R.M.; Brandt, R.A.; Zeelenberg, C.H.; de Jong, B.E.; Timmermans, W.; Azar, L.N.; Hoebe, R.A.; Stallinga, S.; Manders, E.M. Re-scan confocal microscopy: Scanning twice for better resolution. *Biomed. Opt. Express* **2013**, *4*, 2644–2656. [CrossRef]
4. Elliott, A.D. Confocal Microscopy: Principles and Modern Practices. *Curr. Protoc. Cytom.* **2020**, *92*, e68. [CrossRef]
5. Hell, S.W.; Wichmann, J. Breaking the diffraction resolution limit by stimulated emission: Stimulated-emission-depletion fluorescence microscopy. *Opt. Lett.* **1994**, *19*, 780–782. [CrossRef]
6. Willig, K.I.; Rizzoli, S.O.; Westphal, V.; Jahn, R.; Hell, S.W. STED microscopy reveals that synaptotagmin remains clustered after synaptic vesicle exocytosis. *Nature* **2006**, *440*, 935–939. [CrossRef] [PubMed]
7. Gustafsson, M.G. Surpassing the lateral resolution limit by a factor of two using structured illumination microscopy. *J. Microsc.* **2000**, *198*, 82–87. [CrossRef]
8. Gustafsson, M.G. Nonlinear structured-illumination microscopy: Wide-field fluorescence imaging with theoretically unlimited resolution. *Proc. Natl. Acad. Sci. USA* **2005**, *102*, 13081–13086. [CrossRef] [PubMed]
9. Betzig, E.; Patterson, G.H.; Sougrat, R.; Lindwasser, O.W.; Olenych, S.; Bonifacino, J.S.; Davidson, M.W.; Lippincott-Schwartz, J.; Hess, H.F. Imaging intracellular fluorescent proteins at nanometer resolution. *Science* **2006**, *313*, 1642–1645. [CrossRef]
10. Rust, M.J.; Bates, M.; Zhuang, X. Sub-diffraction-limit imaging by stochastic optical reconstruction microscopy (STORM). *Nat. Methods* **2006**, *3*, 793–795. [CrossRef]
11. Wegel, E.; Göhler, A.; Lagerholm, B.C.; Wainman, A.; Uphoff, S.; Kaufmann, R.; Dobbie, I.M. Imaging cellular structures in super-resolution with SIM, STED and Localisation Microscopy: A practical comparison. *Sci. Rep.* **2016**, *6*, 27290. [CrossRef]
12. Allen, J.R.; Ross, S.T.; Davidson, M.W. Structured illumination microscopy for superresolution. *Chemphyschem A Eur. J. Chem. Phys. Phys. Chem.* **2014**, *15*, 566–576. [CrossRef] [PubMed]
13. Fiolka, R.; Shao, L.; Rego, E.H.; Davidson, M.W.; Gustafsson, M.G. Time-lapse two-color 3D imaging of live cells with doubled resolution using structured illumination. *Proc. Natl. Acad. Sci. USA* **2012**, *109*, 5311–5315. [CrossRef] [PubMed]
14. Rego, E.H.; Shao, L. Practical structured illumination microscopy. *Methods Mol. Biol.* **2015**, *1251*, 175–192. [CrossRef]
15. Phillips, M.J.; Voeltz, G.K. Structure and function of ER membrane contact sites with other organelles. *Nat. Rev. Mol. Cell Biol.* **2016**, *17*, 69–82. [CrossRef] [PubMed]
16. Eisenberg-Bord, M.; Shai, N.; Schuldiner, M.; Bohnert, M. A Tether Is a Tether Is a Tether: Tethering at Membrane Contact Sites. *Dev. Cell* **2016**, *39*, 395–409. [CrossRef]
17. Bonifacino, J.S.; Neefjes, J. Moving and positioning the endolysosomal system. *Curr. Opin. Cell Biol.* **2017**, *47*, 1–8. [CrossRef]
18. Benador, I.Y.; Veliova, M.; Mahdaviani, K.; Petcherski, A.; Wikstrom, J.D.; Assali, E.A.; Acín-Pérez, R.; Shum, M.; Oliveira, M.F.; Cinti, S.; et al. Mitochondria Bound to Lipid Droplets Have Unique Bioenergetics, Composition, and Dynamics that Support Lipid Droplet Expansion. *Cell Metab.* **2018**, *27*, 869–885.e866. [CrossRef]
19. Zhang, H.; Wang, Y.; Li, J.; Yu, J.; Pu, J.; Li, L.; Zhang, H.; Zhang, S.; Peng, G.; Yang, F.; et al. Proteome of skeletal muscle lipid droplet reveals association with mitochondria and apolipoprotein a-I. *J. Proteome Res.* **2011**, *10*, 4757–4768. [CrossRef]
20. Valm, A.M.; Cohen, S.; Legant, W.R.; Melunis, J.; Hershberg, U.; Wait, E.; Cohen, A.R.; Davidson, M.W.; Betzig, E.; Lippincott-Schwartz, J. Applying systems-level spectral imaging and analysis to reveal the organelle interactome. *Nature* **2017**, *546*, 162–167. [CrossRef]
21. Li, L.; Zhang, H.; Wang, W.; Hong, Y.; Wang, J.; Zhang, S.; Xu, S.; Shu, Q.; Li, J.; Yang, F.; et al. Comparative proteomics reveals abnormal binding of ATGL and dysferlin on lipid droplets from pressure overload-induced dysfunctional rat hearts. *Sci. Rep.* **2016**, *6*, 19782. [CrossRef]
22. Kalashnikova, M.M.; Fadeeva, E.O. [Ultrastructural study of liver cells from rooks living in ecologically unfavorable areas]. *Biol. Bull. Russ. Acad. Sci.* **2006**, *33*, 99–106. [CrossRef]
23. Sturmey, R.G.; O'Toole, P.J.; Leese, H.J. Fluorescence resonance energy transfer analysis of mitochondrial:lipid association in the porcine oocyte. *Reproduction* **2006**, *132*, 829–837. [CrossRef] [PubMed]
24. Haemmerle, G.; Moustafa, T.; Woelkart, G.; Büttner, S.; Schmidt, A.G.; Weijer, T.v.d.; Hesselink, M.K.C.; Jaeger, D.; Kienesberger, P.C.; Zierler, K.A.; et al. ATGL-mediated fat catabolism regulates cardiac mitochondrial function via PPAR-α and PGC-1. *Nat. Med.* **2011**, *17*, 1076–1085. [CrossRef] [PubMed]
25. Shaw, C.S.; Jones, D.A.; Wagenmakers, A.J. Network distribution of mitochondria and lipid droplets in human muscle fibres. *Histochem. Cell Biol.* **2008**, *129*, 65–72. [CrossRef]
26. Cui, L.; Liu, P. Two Types of Contact Between Lipid Droplets and Mitochondria. *Front. Cell Dev. Biol.* **2020**, *8*, 618322. [CrossRef]
27. Pu, J.; Ha, C.W.; Zhang, S.; Jung, J.P.; Huh, W.K.; Liu, P. Interactomic study on interaction between lipid droplets and mitochondria. *Protein Cell* **2011**, *2*, 487–496. [CrossRef]
28. Young, L.J.; Ströhl, F.; Kaminski, C.F. A Guide to Structured Illumination TIRF Microscopy at High Speed with Multiple Colors. *J. Vis. Exp.* **2016**, *111*, e53988. [CrossRef]

29. Tianyu, Z.; Xing, Z.; Dan, D.; Jia, Q.; Zhaojun, W.; Ming, L.; Baoli, Y.; Lei, M. Polarization control methods in structured illumination microscopy. *Acta Phys. Sin.* **2017**, *66*, 148704. [CrossRef]
30. Förster, R.; Lu-Walther, H.-W.; Jost, A.; Kielhorn, M.; Wicker, K.; Heintzmann, R. Simple structured illumination microscope setup with high acquisition speed by using a spatial light modulator. *Opt. Express* **2014**, *22*, 20663–20677. [CrossRef]
31. Markwirth, A.; Lachetta, M.; Mönkemöller, V.; Heintzmann, R.; Hübner, W.; Huser, T.; Müller, M. Video-rate multi-color structured illumination microscopy with simultaneous real-time reconstruction. *Nat. Commun.* **2019**, *10*, 4315. [CrossRef] [PubMed]
32. Terui, Y. Image processing for structured illumination microscopy. In Proceedings of the 2015 14th Workshop on Information Optics (WIO), Kyoto, Japan, 1–5 June 2015; pp. 1–3. [CrossRef]
33. Wicker, K.; Mandula, O.; Best, G.; Fiolka, R.; Heintzmann, R. Phase optimisation for structured illumination microscopy. *Opt. Express* **2013**, *21*, 2032–2049. [CrossRef] [PubMed]
34. Cao, R.; Chen, Y.; Liu, W.; Zhu, D.; Kuang, C.; Xu, Y.; Liu, X. Inverse matrix based phase estimation algorithm for structured illumination microscopy. *Biomed. Opt. Express* **2018**, *9*, 5037–5051. [CrossRef]
35. Lu-Walther, H.W.; Kielhorn, M.; Förster, R.; Jost, A.; Wicker, K.; Heintzmann, R. fastSIM: A practical implementation of fast structured illumination microscopy. *Methods Appl. Fluoresc.* **2015**, *3*, 014001. [CrossRef] [PubMed]
36. Nieuwenhuizen, R.P.; Lidke, K.A.; Bates, M.; Puig, D.L.; Grünwald, D.; Stallinga, S.; Rieger, B. Measuring image resolution in optical nanoscopy. *Nat. Methods* **2013**, *10*, 557–562. [CrossRef] [PubMed]
37. Huang, X.; Fan, J.; Li, L.; Liu, H.; Wu, R.; Wu, Y.; Wei, L.; Mao, H.; Lal, A.; Xi, P.; et al. Fast, long-term, super-resolution imaging with Hessian structured illumination microscopy. *Nat. Biotechnol.* **2018**, *36*, 451–459. [CrossRef] [PubMed]
38. Garcia-Parajo, M.F.; Segers-Nolten, G.M.J.; Veerman, J.-A.; Greve, J.; van Hulst, N.F. Real-time light-driven dynamics of the fluorescence emission in single green fluorescent protein molecules. *Proc. Natl. Acad. Sci. USA* **2000**, *97*, 7237–7242. [CrossRef]
39. Wang, T.; Jin, M.J.; Li, L.K. [The GTP-Bound form of Rab3D Promotes Lipid Droplet Growth in Adipocyte]. *Mol. Biol.* **2022**, *56*, 564–573. [CrossRef]
40. Cui, L.; Mirza, A.H.; Zhang, S.; Liang, B.; Liu, P. Lipid droplets and mitochondria are anchored during brown adipocyte differentiation. *Protein Cell* **2019**, *10*, 921–926. [CrossRef]

Disclaimer/Publisher's Note: The statements, opinions and data contained in all publications are solely those of the individual author(s) and contributor(s) and not of MDPI and/or the editor(s). MDPI and/or the editor(s) disclaim responsibility for any injury to people or property resulting from any ideas, methods, instructions or products referred to in the content.